ERROR ESTIMATES OF ELASTIC TENSOR COMPONENTS IN STRESS-DEPENDENT VTI MEDIA

Kyle T. Spikes

Department of Geological Sciences
The University of Texas at Austin

ABSTRACT

This work examines the range of physically acceptable VTI stress tensor components for a laboratory shale dataset. The importance of this work is to demonstrate the potential model-based variability and associated error of elastic compliance and stiffness components that are physically acceptable. Laboratory data and a statistical rock physics approach provide the basis for this study. Velocity measurements made as a function of pressure on a low porosity, hard shale provide the basis for completing this work. In terms of a rock physics model, a pressure-dependent model was used to represent simultaneously five compliances at any given pressure from 20–70 MPa. This model requires specifying compliances at high pressure (5 independent parameters), plus four others. These four are a characteristic pressure, the ratio of tangential to normal compliance, the anisotropic crack orientation parameter, and the product of the tangential compliance and the specific surface area of cracks per unit volume. Prior distributions of the five compliance components and the rock physics model provided the parameter space. Acceptable solutions were constrained to several criteria including energy requirements, relative values of stiffness coefficients, and relative values of calculated anisotropic parameters. Multiple solutions were validated, and criterion relating compressional to shear waves was violated most frequently. Differences between the models and data indicate error in the data or that the samples deviate away from a true VTI medium. These simulations provide a way to analyze the elastic tensor components, and they provide uncertainty estimates that could be incorporated into seismic inversion, imaging, and numerical modeling schemes.

INTRODUCTION

This work is a study of the range of physically acceptable TI stress tensor components based on a laboratory shale dataset. It includes a statistical rock physics formulation of a model and analysis of the potential uncertainty in the data and the model. More specifically, the results provide justification to assign error bars to the data. These error bars can be associated either to measurement error or deviations away from true VTI behavior of the sample. Both situations might be present, but the proportion of each remains unknown. The importance of this work

pertaining to shales is that it provides some useful ranges of the elastic tensor components and standard anisotropy parameters. The application presented here is to laboratory data. Extensions to well-log and seismic data are quite important. These include rock-property prediction (including texture) and imaging scenarios where anisotropic migration might become critical in identifying productive zones. In particular, the appropriate ranges of the elastic coefficients and anisotropy parameters can be constrained and then used in seismic applications.

The data used in this work come from Wang (2002). The rock physics model is pressure dependent and represents simultaneously five compliance coefficients at any given pressure from 20–70 MPa (Pervukhina et al., 2011). The new contribution consists of adding uncertainty analysis to the modeling and computing multiple solutions. Those solutions are constrained to several criteria including energy requirements, relative values of stiffness coefficients, and relative values of anisotropy parameters. These criteria are relatively well known, but considering multiple possible solutions within some range of uncertainty has not been done to any extent. Similar work consists of applying the ANNIE approximations (Schoenberg et al., 1996) as in e.g., Ostadhassan et al. (2012).

Modeling pressure-dependent laboratory velocities has been shown to be very useful (Stierman et al., 1979; Eberhart-Phillips et al., 1989; Zimmerman, 1991; Prasad and Manghnani, 1997; Kaselow and Shapiro, 2003; Shapiro, 2003; Siggins and Dewhurst, 2003). These approaches were for clastic and carbonate rocks, primarily for isotropic scenarios, for which exponential fitting terms related the velocity to effective stress. However, anisotropic characterization of shales is quite important, not least because of the increase in interest of extracting hydrocarbons from inherently anisotropic shales and mudstones (Vernik and Liu, 1997; Sayers, 1994, 2005, 2012; Horne et al., 2012; Madadi et al., 2013). Typically, these rocks are assumed to be inherently transversely isotropic due to the alignment of elongated clay minerals, aligned elongated pores, and because those clay minerals are themselves transversely anisotropic. The effective symmetry that results most often is vertical transverse isotropy (VTI). Results from this study indicate possible systematic data error and/or deviations from homogeneous VTI behavior.

Energy requirements and relative values elastic constants

In a transversely isotropic medium, we require five independent elastic constants to specify the directionally dependent velocities. In terms of the components c_{ij} (i, j = 1:6) of the stiffness matrix using the familiar Voigt notation, the five constants that are required are c_{11}, c_{33}, c_{44}, c_{66}, and c_{13}, where $c_{12} = c_{11} - 2c_{66}$ (Equation 1).

$$c_{ij} = \begin{bmatrix} c_{11} & c_{12} & c_{13} & 0 & 0 & 0 \\ c_{12} & c_{11} & c_{13} & 0 & 0 & 0 \\ c_{13} & c_{13} & c_{33} & 0 & 0 & 0 \\ 0 & 0 & 0 & c_{44} & 0 & 0 \\ 0 & 0 & 0 & 0 & c_{44} & 0 \\ 0 & 0 & 0 & 0 & 0 & c_{66} \end{bmatrix} \tag{1}$$

Equation 1 can be used to specify either vertically transverse isotropy (VTI) or horizontal transverse isotropy (HTI) depending on the symmetry axis. Continuing with that notation, directions must be defined, and the x_3 axis is taken as the vertical axis (the symmetry axis) in Figure 1 for a VTI medium.

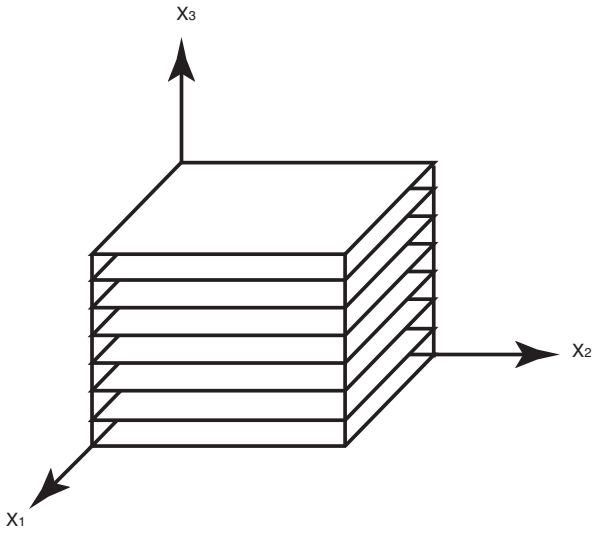

Figure 1. Schematic of a medium with homogeneous VTI symmetry. Elastic tensor values are symmetric around the x_3 axis.

Very specific energy considerations require additional relationships among some of the non-zero c_{ij} components. Specifically, those considerations are (Mavko et al., 2009)

$$c_{44} \geq 0, \tag{2}$$

$$c_{11} > |c_{12}|, \tag{3}$$

$$(c_{11} + c_{12})c_{33} \geq 2c_{13}^2, \text{ and} \tag{4}$$

$$(c_{13} + c_{44}) > 0. \tag{5}$$

These stiffness components and their inequalities arise in the Thomsen (1986) parameters, ε, γ, and δ (Equations 6–9) for weak anisotropy.

$$\varepsilon = \frac{c_{11} - c_{33}}{2c_{33}} \tag{6}$$

$$\gamma = \frac{c_{66} - c_{44}}{2c_{44}}. \tag{7}$$

$$\delta = \frac{(c_{13} + c_{44})^2 - (c_{33} - c_{44})^2}{2c_{33}(c_{33} - c_{44})}. \tag{8}$$

Furthermore, in terms of the Thomsen (1986) parameters, Grechka et al. (1999) and Tsvankin (2001) established additional constraints. Those constraints or relative values of the anisotropy terms are

$$\delta \geq -\frac{1}{2}(1 - \frac{c_{44}}{c_{33}}) \tag{9}$$

$$\delta \leq \frac{2}{c_{33}/c_{44} - 1} \tag{10}$$

$$\varepsilon > \delta \tag{11}$$

$$\varepsilon - \delta \geq 0 \tag{12}$$

$$\gamma \geq 0 \tag{13}$$

All these energy and relative values of the stiffness elements are satisfied in this work. Additional criteria were imposed in terms absolute maximum values for c_{11}, c_{33}, c_{44}, and c_{66}. If either c_{11} or c_{33} exceeded 100 GPa, the solution for the entire pressure range was discarded. Similarly, if a value of 50 GPa was reached for either c_{44} or c_{66} that solution was eliminated.

LABORATORY SHALE DATA

The data set used comes from Wang (2002) who measured several different shale samples. The one of particular interest is the G3 brine-saturated hard shale. Table 1 shows for this sample

its porosity, density, effective pressure, VTI stiffness components, and anisotropy values. This sample came from a depth of 3512 m. Pore pressure in the experiment was constant at 6.90 MPa.

Table 1. Measured properties of the G3 hard shale sample from Wang (2002). Values include porosity, density, effective stress, five VTI elastic coefficients, and anisotropy terms.

Porosity %	Density g/cm^3	Eff. Stress MPa	c_{11} GPa	c_{33} GPa	c_{44} GPa	c_{66} GPa	c_{13} GPa	ε	δ	γ
4.12	2.605	20.69	54.42	36.18	14.73	20.23	7.94	0.252	0.035	0.187
4.12	2.605	34.48	55.32	37.40	14.95	20.36	8.35	0.240	0.023	0.181
4.12	2.605	44.82	56.09	38.40	15.12	20.48	8.71	0.230	0.015	0.177
4.12	2.605	55.17	56.98	39.67	15.34	20.63	9.30	0.218	0.008	0.172

The data from Wang (2002) are stiffness coefficients and subsequently computed anisotropy parameters. The rock physics model, however, is a function of compliances. Furthermore, the energy conditions are functions of stiffness. To determine if the solutions should exist, the models must be converted to stiffness values from compliance values. That conversion is given in Equations 14–18. Stiffness and compliance coefficients, for both the model and the data, are examined in the results. Table 2 contains the corresponding compliance tensor component values.

$$s_{11} + s_{12} = \frac{c_{33}}{c_{33}(c_{11} + c_{12}) - 2c_{13}^2} \tag{14}$$

$$s_{11} - s_{12} = \frac{1}{c_{11} - c_{12}^2} \tag{15}$$

$$s_{13} = -\frac{c_{13}}{c_{33}(c_{11} + c_{12}) - 2c_{13}^2} \tag{16}$$

$$s_{33} = \frac{c_{11} + c_{12}}{c_{33}(c_{11} + c_{12}) - 2c_{13}^2} \tag{17}$$

$$s_{44} = \frac{1}{c_{44}} \tag{18}$$

Table 2. Calculated compliance tensor values using Equations 14–18 from the stiffness tensor coefficients for the G3 brine-saturated hard shale in Wang (2002).

Eff. Stress (MPa)	s_{11} GPa^{-1}	s_{33} GPa^{-1}	s_{44} GPa^{-1}	s_{66} GPa^{-1}	s_{13} GPa^{-1}
20.69	0.0200	0.0291	0.0679	0.0494	–0.00339
34.48	0.0198	0.0282	0.0669	0.0491	–0.00337
44.82	0.0196	0.0276	0.0661	0.0488	–0.00337
55.17	1.0194	0.0268	0.0652	0.0485	–0.00343

These measurements, which are extremely difficult to make in some cases, are inherently uncertain. These measurements depend on many factors, including preservation of the samples, frequency, pore fluid, transducer-to-sample coupling, and the picking of first arrivals on waveforms. Assigning error bars to each measurement is an arduous task, and ultimately these error bars are estimates themselves. Arguably, the error bars increase for smaller effective pressure values (less than ~20 MPa), and they should decrease as pressure increases. Wang (2002) provided estimates of these error bars. The stated errors for the anisotropy values were approximately 10% for ε and γ and 25% for δ. For velocities, these were smaller, amounting to 1% for P and SH-wave velocities and about 2% for SV-wave velocities. These translate into 1–6% error for compliance or stiffness values. The assigned error bars used here are consistent with these estimated values. Table 3 gives the error bars in terms of percent of the either the stiffness or compliance coefficient value. The size of the error bars was chosen to vary from ±5% the compliance value at low stress to ±2% at high stress for the compliance components s_{11}, s_{33}, and s_{44}. For s_{66}, the high-pressure value was 1%. For s_{13}, the range is ±20% at low pressure and ±10% at high pressure, decreasingly linearly (see Table 2). For the c_{ij} values, ±2% and ±0.8% were used for c_{11} and c_{33}; ±5–2% for c_{44}; ±5–1% for c_{66}; and ±20–10% for c_{13}. The relatively large values for s_{13} and c_{13} were used because they have the most uncertainty due to the requisite P-wave measurement at 45° to the symmetry axis.

Table 3. Error bar sizes for compliance and stiffness tensor values as a function of pressure EB% stands for the percent of the compliance or stiffness value at the respective pressures.

Eff. Stress (MPa)	s_{11} EB%	s_{33} EB%	s_{44} EB%	s_{66} EB%	s_{13} EB%	c_{11} EB%	c_{33} EB%	c_{44} EB%	c_{66} EB%	c_{13} EB%
20.69	5.0	5.0	5.0	5.0	20.0	2.0	2.0	5.0	5.0	20.0
34.48	4.0	4.0	4.0	3.6	16.6	1.6	1.6	4.0	3.6	16.6
44.82	3.0	3.0	3.0	2.3	13.3	1.2	1.2	3.0	2.3	13.3
55.17	2.0	2.0	2.0	1.0	10.0	0.8	0.8	2.0	10.0	10.0

ROCK PHYSICS MODEL

The stress-dependent behavior of elastic components for the shale sample under consideration can be modeled in various ways. One approach is through the argument of closing elongated pores with increasing closing stress. This can be done by modeling aspect ratios and crack densities as a function of effective pressure (Spikes, 2011; Sava, 2004). The way considered here is through an excess compliance method (Sayers and Kachanov, 1995; Ciz and Shapiro, 2009; Pervuhkina et al., 2011; Kao and Gibson, 2012). It focuses on the important pressure range of 20–80 MPa. A clear advantage is the ability to model the stress-dependency of VTI compliance tensor elements. A disadvantage, naturally tied to the symmetry of a VTI system, is the number of parameters required to fit simultaneously the five measurements. Pervukhina et al. (2011) indicate that a related model from Ciz and Shapiro (2009) is a specific solution to the general problem in Pervukhina et al. (2011). The Pervukhina et al. (2011) approach requires one fewer parameter than does Ciz and Shapiro (2009).

For the Pervukhina et al. (2011) model, explicit forms for the s_{ij} values are specified using the excess compliance approach (Sayers and Kachanov, 1995). This effective compliance is a function of compliance at high stress where all low aspect ratio voids should be closed (i.e., the asymptotic behavior of compliance or stiffness at high pressure) and an exponential term to account for the excess compliance. Equations 19–23 give the formulations for the five independent compliance values. In these equations, Δs_{ij} are the excess compliances, s_{ij} are the effective compliances, s_{ij}^0 are the high-pressure compliances, and P is pressure. Four additional coefficients ($s_n B_T$, B, η, and P_c) satisfy the simultaneous solving for the effective compliance. These four are, respectively, the product of the tangential compliance and the specific surface area of cracks per unit volume, the ratio of tangential to normal compliance, the anisotropic crack orientation parameter, and the characteristic pressure at which all compliant fractures are closed. The change in compliance as a function of pressure is an inverse exponential function that controls the local slope of the model. The other four parameters affect the zero-pressure endpoint and the average slope.

$$\Delta s_{11} = s_{11} - s_{11}^0 = \frac{s_n B_T \exp(-P/P_c)}{105}(14 + 4\eta + 21B + 3B\eta) \tag{19}$$

$$\Delta s_{33} = s_{33} - s_{33}^0 = \frac{s_n B_T \exp(-P/P_c)}{105}(14 + 6\eta + 21B + 15B\eta) \tag{20}$$

$$\Delta s_{44} = s_{44} - s_{44}^0 = \frac{s_n B_T \exp(-P/P_c)}{105}(42 + 16\eta + 28B + 12B\eta) \tag{21}$$

$$\Delta s_{66} = s_{66} - s_{66}^0 = \frac{s_n B_T \exp(-P/P_c)}{105}(42 + 10\eta + 28B + 4B\eta) \tag{22}$$

$$\Delta s_{13} = s_{13} - s_{13}^0 = \frac{s_n B_T \exp(-P/P_c)}{105}(7B + 3B\eta - 7 - 3\eta) \tag{23}$$

This model relies on a non-linear fitting routine (Marquardt-Levenberg) to fit simultaneously all the necessary coefficients at any given pressure. However, it is not demonstrated in either of the papers that there is an internal check within the fitting routine to ensure the energy requirements. This may not seem that significant because the fits to the published data are quite good. However, I show that a sizeable fraction of solutions, obtained from perturbing the coefficients within some error range, cannot exist. When we assume that uncertainty exists in the measurements, then we can justify a set of solutions to the non-linear fitting. We can limit that set of solutions, however, by ensuring the constraints, and rejecting those that violate these constraints. This can serve two purposes: 1) characterizing the uncertainty in the measurements, and 2) possibly seeing where they might deviate from homogeneous VTI symmetry.

In the proper circumstances, these models can be useful. However, care must be taken as to avoid any calculations (at any pressure) that violate the stated mandates for a true VTI material. If the model calculations violate these conditions, but represent the data well, then those data points might not necessarily belong to a truly VTI material. This would be the case of using a VTI model to fit data that is of higher order symmetry and/or heterogeneous. On the other hand, these models could be used to identify errors in the measurements. By simulating numerous values and selecting the ones that can exist, as was done here, we can begin to the use the models potentially in ways that they were not originally intended. More specifically, as long as the model solutions exist, they represent a possible subset of all solutions that represent the data and the associated uncertainty with those data measurements.

Figure 2 (left column) contains the compliance data values (inverted using Equations 14–18) and the assigned error bars in black. These are the compliance and pressure values from Table 2 and the error bar values from Table 3. The gray line in each frame is the best-fit model determined from the non-linear least squares fitting routine (Levenberg-Marquardt). The routine works by simultaneously fitting all five compliances at a given pressure using the s_{ij}^0 as an input as well and then finding $s_n B_T$, B, η, and P_c values with a specified tolerance to match the data. All fits of the model to the data are a reproduction of those published in Pervukhina et al. (2011).

Table 4 contains the values for all the coefficients. The difference between Figure 2 and those previously published are the addition of the error bars around the data and the inclusion of pressures less than 10 MPa. The model fits the data very well for all compliance components at pressures greater than the 30 MPa. The measurements at 20 MPa are not matched nearly as well as the others. Figure 3 contains the Thomsen (1986) anisotropic parameters ε, γ, and δ. As expected, all three parameters decrease in magnitude with increasing pressure. The quality of the match of the model to the data for ε and δ resemble the matches in Figure 2 above 30 MPa. On the other hand, the match to γ appears to be quite good. However, it will be shown more clearly later that the model does not accurately predict the expected drop in γ as pressure increases.

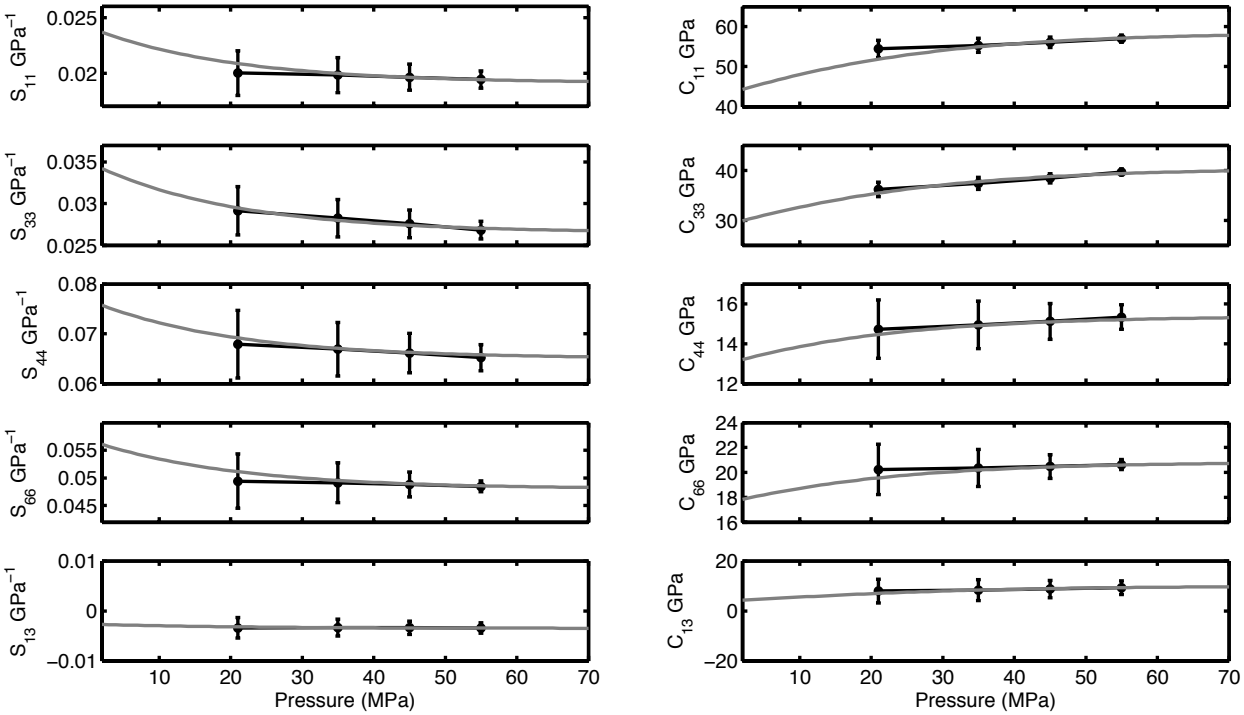

Figure 2. Plots of compliance (left column) and stiffness components (right column) as a function of pressure. The data from Wang (2002) are plotted in black along with the assigned error bars (Table 3). Gray lines are the best-fit model for the compliance values determined simultaneously at each pressure. The gray lines in the right column were inverted from those on the left. The models explain well the elastic components for pressures greater than 30 MPa.

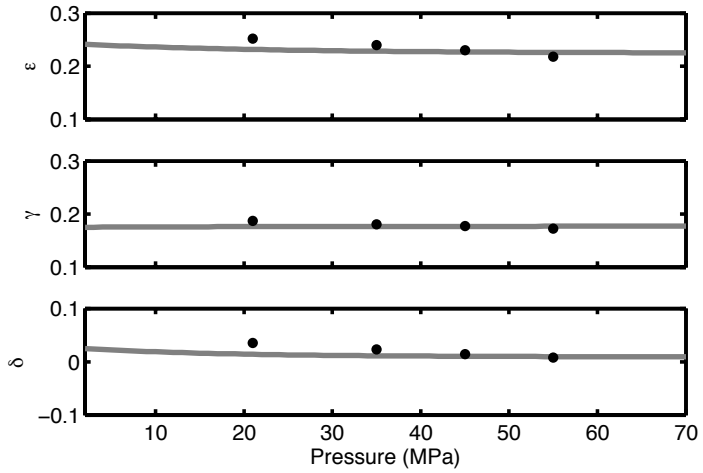

Figure 3. Anisotropic parameters as a function of pressure. The data, black points without error bars, indicate decreasing anisotropy with increasing effective stress, as expected. The epsilon and delta fits to the data resemble those in Figure 2 in which the best fits occur at pressures greater than 30 MPa. For gamma, the fit appears to be quite good. Although it is not obvious in this figure, the gamma model line increases with effective stress, counter to the expected trend.

Table 4. Model parameters for the best-fit models displayed in Figures 2 and 3.

s_{11}^0 GPa^{-1}	s_{33}^0 GPa^{-1}	s_{44}^0 GPa^{-1}	s_{66}^0 GPa^{-1}	s_{13}^0 GPa^{-1}	$s_n B_T$	B	η	P_c MPa
0.0191	0.0265	0.0650	0.0480	–0.0035	0.007	2	2	20

NUMERICAL MODELING

The numerical modeling performed here accounts for the energy requirements, the relative values of the stiffness elements, and the inequalities of the anisotropy parameters. Directional pressure considerations are also considered. In particular, if a VTI material is exposed to a hydrostatic stress, the resulting symmetry of the stressed VTI material is also VTI. If that same unstressed VTI material is subject to a uniaxial stress parallel to the symmetry axis, the stressed material will also be VTI (Mavko et al., 2009). For now, only the hydrostatic case is considered, in which all the c_{ij} increase with increasing hydrostatic stress. This hydrostatic stress is assumed to occur in laboratory experiments where samples with different orientations with respect to the symmetry axis bedding are put under the same effective-pressure conditions.

To understand the potential combinations of elastic tensor components that violate one or more of constraints, the numerical modeling started with a set of reference values from the original best-fit model (see Table 4). Compliances at high stress (s_{ij}^0) were left unchanged as were the other four parameters needed to fit the model ($s_n B_T$, B, η, and P_c). Simultaneous perturbations of the s_{ij} values provided the variations over which to consider the existence conditions. More specifically, uniform distributions of s_{11}, s_{33}, and s_{13} were defined (Figure 4a, b, and c). Following these definitions, two-dimensional uniform distributions of s_{44} and s_{66}

provided the parameter space over which to simulate the models. The one-dimensional distributions contained 805 entries. The two-dimensional ones contained 805 x 263 entries. The pressure range considered was to 0–70 MPa, giving an overall number of simulations to consider of 805 x 263 x 71 = 15031765. Each simulated compliance component contains negative values even though the only one that can be negative is s_{13}. The negative values in the other four components resulted from the generation of the distributions. Although they could have been removed prior to calculating and comparing all the resulting components, they were kept in order to provide an additional test of the criteria for the combination of tensor components to exist. Results demonstrate that the algorithm removed these as expected.

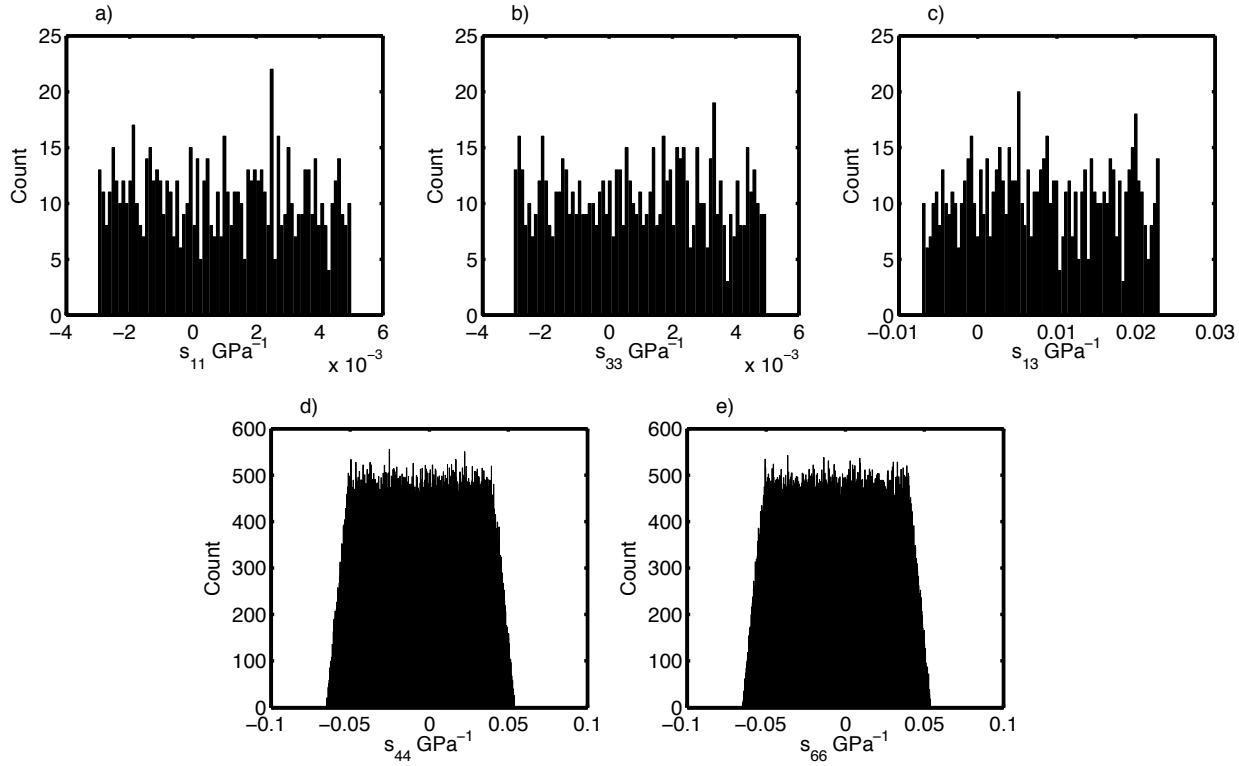

Figure 4. Prior distributions of the compliance components. In a, b, and c are 11, 33, and 13 components, respectively. Each is a one-dimensional uniform distribution. The histograms in d) and e) for the 44 and 66 terms show the values from two-dimensional distributions. Their similarity to each other was intentional primarily due to the small differences in the values of the 44 and 66 components. In the simulations, different values 44 and 66 components were considered as long as their relative values did not violate any energy conditions.

RESULTS

The first set of numerical simulation results (Figure 5) shows the allowable compliances and stiffnesses for subset 118. A subset refers to a collection of the solutions for one range of the

shear compliances. Subset numbers span 1 to 263. The c_{44} and c_{66} components are not shown. First to notice is that many solutions exist, but some of the trends of the stiffness components increase rapidly with increasing pressure. To remove these, local derivatives of the c_{11}, c_{33}, and c_{13} components were computed in the pressure direction. If a derivative of any one of these components exceeded an assigned slope, all five stiffness tensor components, and the corresponding compliances, for all pressures were eliminated. The slopes used for cut off criteria were $dP/dc_{ij} > 1$ for c_{11} and c_{33} and $dP/dc_{ij} > |0.25|$ for c_{13}. Derivatives were not necessary to compute for the other two components. Furthermore, this derivative information was not initially expected. It arose from large and small perturbations of the compliance components. In some cases, the compliance models behaved predictably as a function of pressure. However, their corresponding stiffness models showed the quickly increasing behavior illustrated in Figure 5.

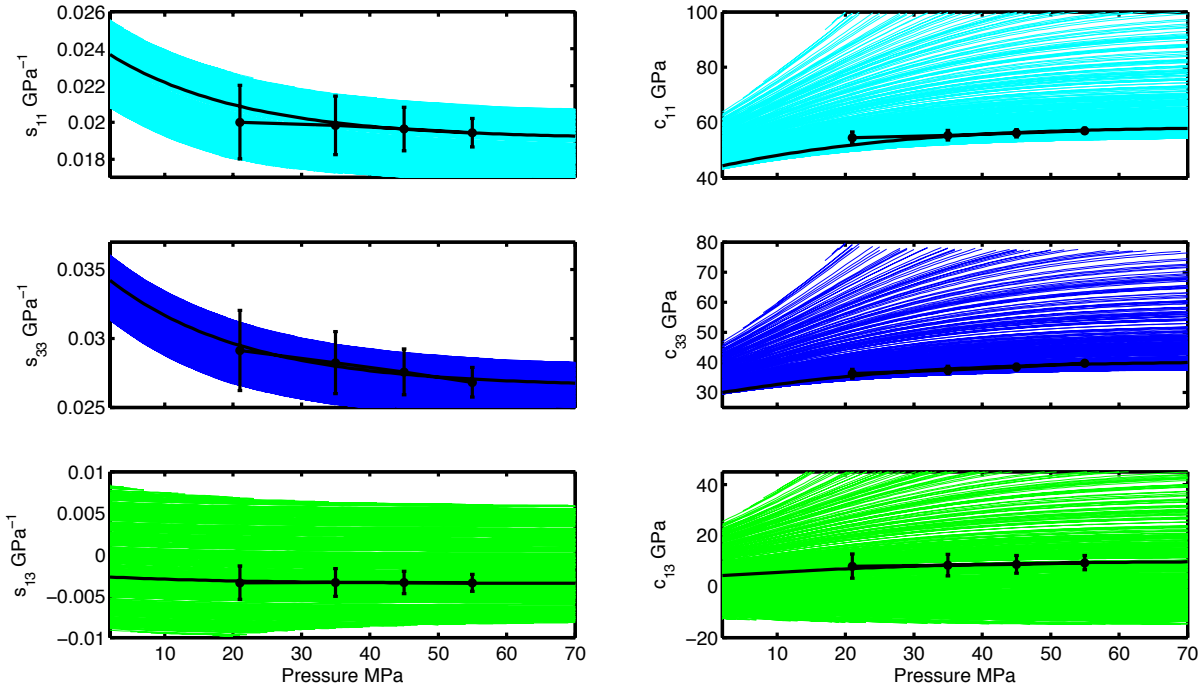

Figure 5. Compliance (left) and stiffness (right) models without considering local slopes of the stiffness components for subset 118. In the compliance components, some models behave expectedly with smooth decreases with increasing pressure. However, many corresponding stiffness solutions rapidly increase with pressure.

Because of the 2D histograms used in the simulations for c_{44} and c_{66}, numerous subsets of solutions exist. They can all be concatenated to provide an overall solution set. However, many of these subsets bear no resemblance to the shale data under consideration, but they indicate allowable combinations of the elastic components. Examining all these solutions subsets will be useful in subsequent work when analyzing potential ranges of the all the elastic components. An illustration of the number of solutions present is shown in Figure 6. This figure shows the

percent of solutions that exist as a function of the solution subset number. The total number of solution subsets is 263. The percentage on the y-axis corresponds to the number of simulations accepted for each solution subset. The number of simulations in each subset is 805x71, where 71 corresponds to the number of pressures. The maximum percentage is ~50% for solution subset 139, meaning approximately 400 solutions exist over all pressures for this subset. Solution subsets 1–80 and 200–263 have no valid entries. No solution subset explained all the compliance and stiffness components simultaneously and equally well for all pressures. The subset analyzed in detail is subset 118 because it provided the best fits overall to the data. Two other subsets are shown later for illustration purposes.

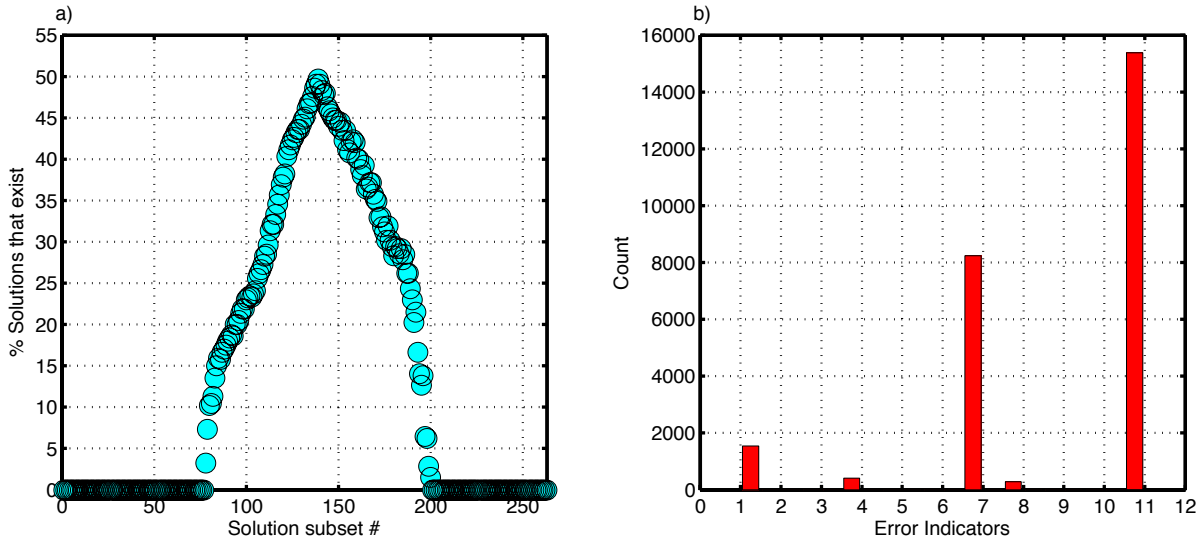

Figure 6. a) Percent of solutions that exist as a function of the solution subset number. The solution subset number refers to the variations of the 44 and 66 tensor terms being varied. The maximum percent is about 50% at subset 139. For percentages of 0, no solutions exist. An increase from 0% to the maximum and back down to 0% depicts how many solutions can exist given the permutations of the elastic coefficients in the simulations. In b), the bar graph indicates the number (count) of each condition that was violated during the simulation for subset #118. Error indicators are 1, 4, 7, 8, and 11. The indicator 1 correspond to Equation 4; indicator 4 corresponds Equation 12; indicator 11 to Equation 5. Indicators 7 and 8 correspond to cut offs of the 11 and 33 stiffness components greater than 100 GPa. The most counts for indicator 11 corresponds to the relative values of c13 and c44, which are typically assumed to sum to greater than zero for most situations when thin laminations are present.

Figure 7 displays all five compliance and stiffness components for the allowable solutions for subset 118. Qualitatively, solution subset 118 best fits the data based on the spread of the allowable solutions compared to the error bars. Approximately 287 solutions exist for all pressures. Multiple criteria were violated during the simulations (Figure 6b). The energy requirement most often violated is $(c_{13}+c_{44})>0$ (Equation 5). Other violations corresponded to Equation 4 and Equation 12 (Figure 6b). In addition, some models were eliminated because the

maximum c_{11} and c_{33} values exceeded 100 GPa, clearly beyond the range of the data even at high pressure as well as the removal of solutions based on the directional derivatives. The data, error bars, and original solution (in black) are identical to those in Figure 2. Because of the uniform distributions used in the simulations, the original model should fall near the center of the simulated models as an expected or average for each component. This expected result does no appear here. Among the five compliance components, s_{11} and s_{33} appear to explain the measurements and error bars most completely with approximately the same number of solutions above and below the original. Similar arguments could be made for the c_{11} and c_{33} components. The allowable solutions for the 44 and 66 terms lie mostly below the original for the compliances and above for the stiffnesses. The opposite is true for the 13 terms. Furthermore, for 13 terms, the number of allowable solutions appears to span a large range, from negative to positive values for all pressures for both s_{13} and c_{13}. This is a very clear illustration of the uncertainty in these terms that are so important for explaining VTI velocities.

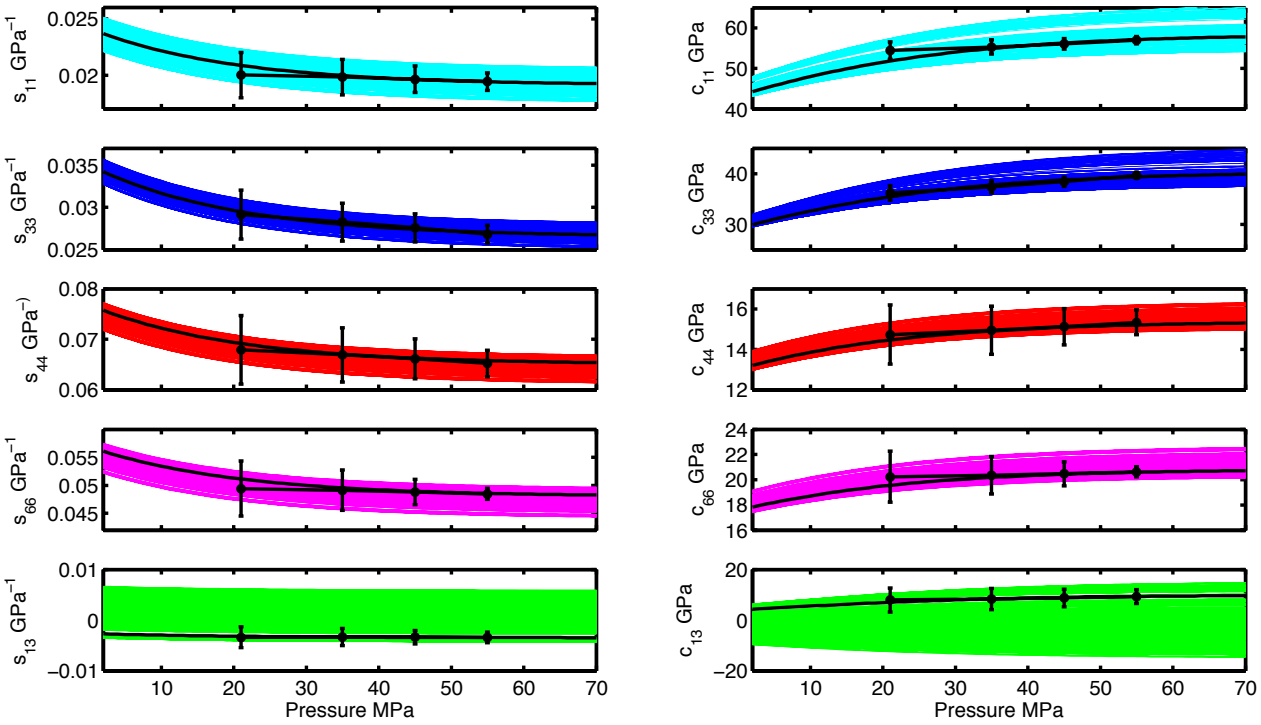

Figure 7. Solutions for the compliance components in the left column and stiffness components in the right column for subset #118 (see Figure 6). A total of 805 simulations over all pressures were considered, and 287 passed on the checks for energy requirements and other cut off criteria. Considering the overall fit of all models to the original model in black, the 11 and 33 terms are likely the best fits, followed by the 44 and 66 terms. However, the 13 terms are skewed notably above (compliance) and below (stiffness) the original model and data. This suggests the sensitivity of this parameter. The inconsistent match of the range of models from one component to the next also suggests that more error is present in the 44, 66, and 13 data than in the 11 and 33 data components. An alternate scenario is that these samples are not absolutely VTI.

Figure 8 contains the corresponding anisotropy parameters to the models in Figure 7. Each is plotted as a function of pressure similar to Figure 3, where the red lines and points correspond to the original model and data, respectively. For the uppermost frame, ε and δ models decrease in value with increasing pressure. For ε, as pressure increases, it appears that different models could easily explain the measurements at the different pressures. For δ, a single model, or at least fewer than for ε, might explain the data. As depicted in Figure 3, the γ data decrease in value with pressure like the other two parameters. A single model fitted to this data appears either flat or decreases slightly with pressure. When viewed with multiple simulations, this figure clearly indicates that the model predicts an increase in γ with pressure. This is not understood yet, but it is no the focus of this paper. All other models behave expectedly, so an error in the algorithm seems unlikely. This issue likely will be explored in future work.

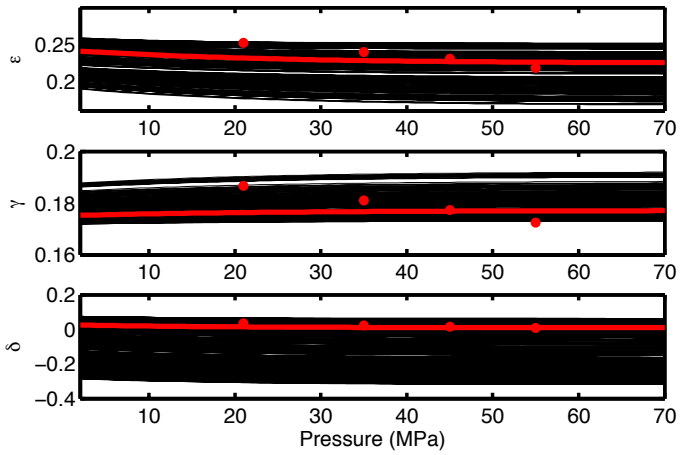

Figure 8. Anisotropy parameters epsilon, gamma, and delta for the allowable models stiffness coefficients (black lines) presented in Figure 7. The data (red points) and original model (red lines) are the same as in Figure 3. As pressure increases, all three data sets decrease in value. The simulations mimic that trend for epsilon and delta. However, the models all indicate an increase in gamma as a function of increasing pressure. The reason is presently unclear. However, this is not observable by looking only at the best fitting model as in Figure 3.

Two other solutions subsets are presented (Figures 9 and 10). In Figure 9, the subset number is 100 (see Figure 6a) and 135 in Figure 10. The s_{11}, s_{33}, and c_{33} models in Figure 9 explain the data relatively well where 184 solutions exist in that subset. However, the other 7 terms do not. Compliances are over predicted and stiffnesses under predicted. Nonetheless, all the models plotted in color are allowable solutions, which give some idea to the possible variability in the VTI medium. On the other hand, in Figure 10, more solutions exist (377) than in Figure 9. However, shear compliances are under predicted and shear stiffnesses over predicted. The reason for this change from Figure 9 to Figure 10 is simply that for the smaller subset numbers, the simulated shear compliances were larger, and they decreased as the subset number increased.

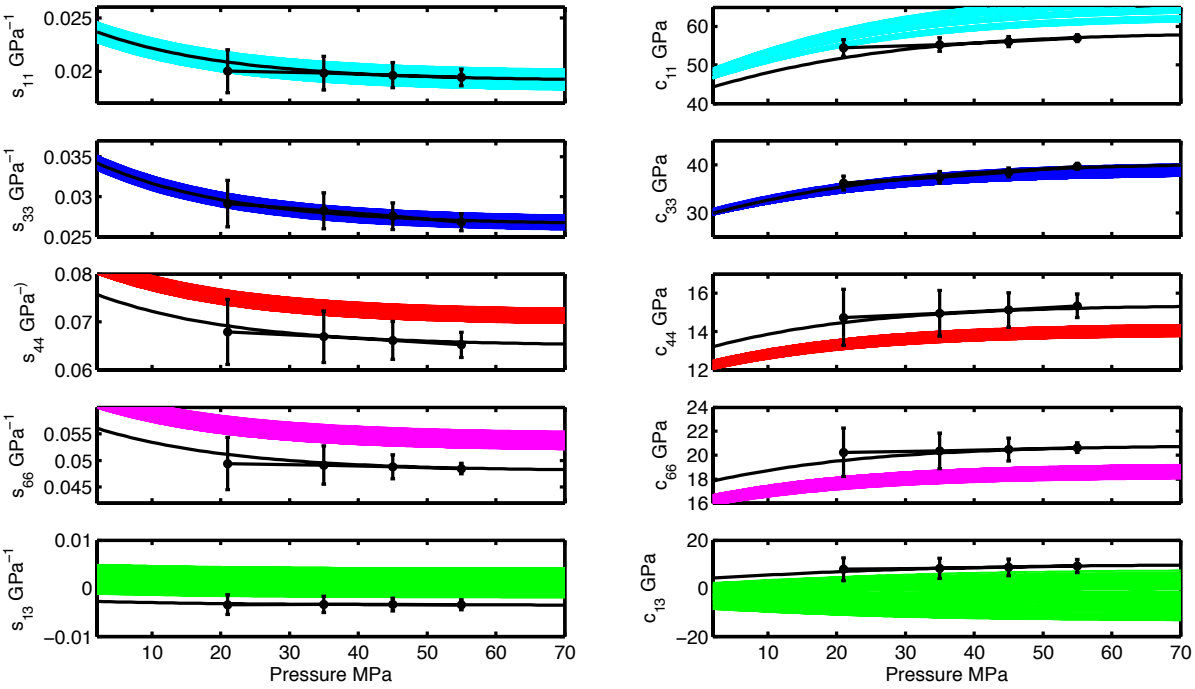

Figure 9. Allowable models for subset 100. The simulated shear compliances fall well above the data and original model whereas the shear stiffnesses fall below them. Three of the ten components match relatively well, namely, the compliance 11 and 33 terms and stiffness 33 term.

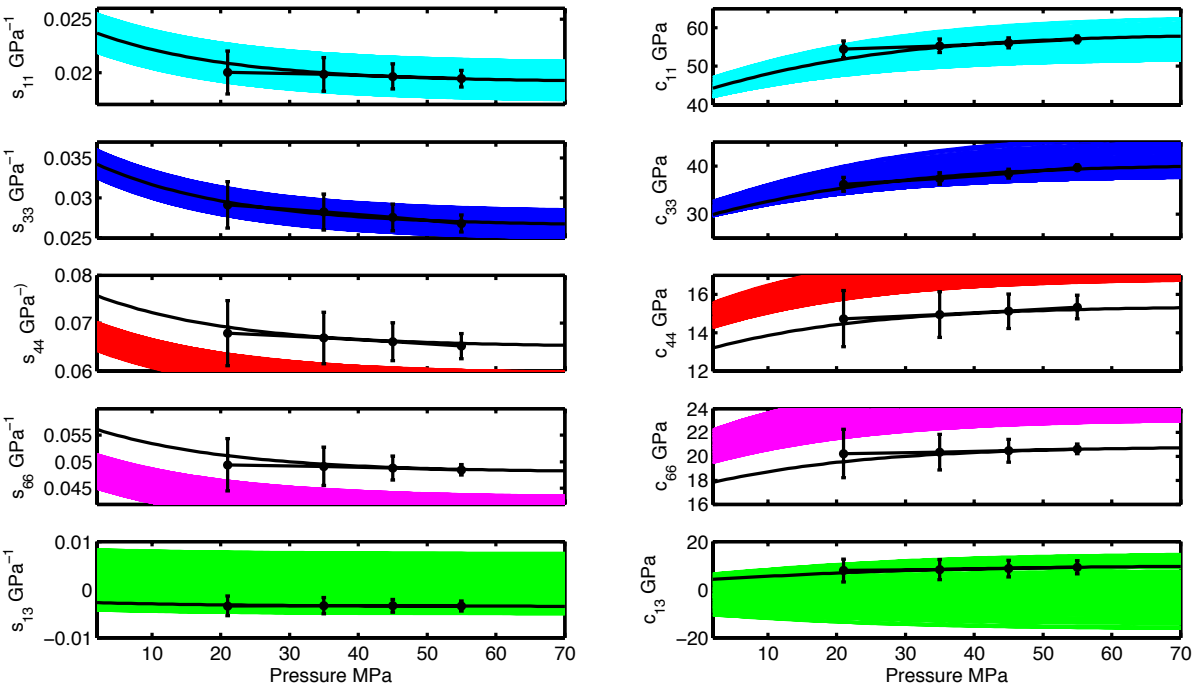

Figure 10. Allowable models for subset 135. Relative to Figure 9, the shear compliances are noticeably under predicted and shear stiffnesses the opposite. The optimal subset (118) plotted in Figure 7 falls in between subsets 100 and 135, where the shear compliances were larger for smaller subset numbers, and these shear compliances decreased as the subset number increased.

DISCUSSION

Examining again Figures 7–9, the most stable solutions correspond to s_{11}, s_{33}, c_{11}, and c_{33}. The s_{13} and c_{13} solutions vary some, but not nearly as much as the pure shear terms. By design, the pure shear terms were intended to vary significantly, but it was not known before the simulations were run that the other terms would appear to be stable. Temporarily ignoring the fits to the data, this means that for a very well known set of directional P-wave measurements, the corresponding directional S-wave measurements might have extremely large possible variations. On the other hand, if at least one directional S-wave component is known, the ability to find a set of anisotropic solutions improves significantly although uncertainty will be present in the s_{13} or c_{13} terms.

Figure 7 illustrated the best fits of all the solution subsets to the data when qualitatively incorporating the added error bars to the data. The P-wave data fit nearly in the center of the models, but the S-wave data and s_{13} and c_{13} terms are clearly skewed to one side or another (depending on compliance or stiffness). An explanation for this is that the S-wave measurements are systematically skewed. Specifically, the stiffness data fall on the low side of the models. This suggests that the S-wave velocity measurements could be systematically low. The same argument could be made of the c_{13} term, where the P-wave velocity at 45° could be systematically fast. Wang (2002) indicated a possible 3% systematic error in the experimental set up and travel time picking routine. The simulations shown here could be an indicator of that experimental error.

A separate interpretation can also be made regarding the medium itself. Figure 1 illustrates a relatively simple medium even though that medium requires five independent elastic constants for a complete description. The simplicity of that medium is in regards to being a truly homogeneous VTI medium. The measurements made on the sample used in this paper assumed that the medium was indeed VTI. This is likely a very fair assumption based on the descriptions of the samples. However, at the frequency of the measurements (MHz range), inhomogeneities could start to express themselves. These expressions could be different for P-waves versus S-waves. Therefore, the alternative interpretation to systematic data error is that that medium itself is not a truly homogeneous VTI medium. These two interpretations cannot be resolved completely at this time. Numerical modeling of different samples should be performed to determine better if one or the other of the interpretations is indeed correct.

CONCLUSIONS

Statistical modeling of laboratory data showed some inconsistencies between the best fitting solutions among the elastic tensor components. The interpretations for this misfit are that systematic errors occurred in the measurements (S-wave in particular), or that the medium was VTI but not homogeneous. These two interpretations cannot be verified without additional testing on different datasets, including possible synthetic materials where the nature of the medium can be controlled. Original fits of this rock physics model to the same dataset (Figures 2 and 3) do not suggest either of these interpretations. Only with the numerical simulations over ranges of the elastic components can these conclusions be drawn. Additionally, the identification of gamma models increasing with pressure would not be recognized without the simulations. Regardless, the simulations provide ranges of the anisotropy parameters that could be included in seismic modeling, inversion, and imaging schemes. Because these anisotropy values are not known very well during the imaging and modeling steps, viable ranges of them would be quite useful a priori. For seismic inversion schemes, narrow ranges of the anisotropy values could be invoked to help match synthetic to real data. Finally, the numerical scheme presented here could be used at the laboratory scale to help pick velocities from acoustic or elastic signals. The results here showed stable solutions exist for the P-wave components. While S-wave and P-wave measurements at 45° are being made, simulated ranges of these values could be used to help guide the picking of transit-time signals within some prescribed error range. The model used in here or a different one could be used. If the picked travel times do not necessarily change during this comparison but deviate from an expected value, then that would likely indicate heterogeneity.

ACKNOWLEDGEMENTS

The Exploration and Development Geophysics Education and Research (EDGER) Forum at The University of Texas at Austin partially supported this research.

REFERENCES

Avseth, P., T. Mukerji, and G. Mavko, 2005, Quantitative seismic interpretation: Applying rock physics tools to reduce interpretation risk: Cambridge University Press.

Ciz R. and S. A. Shapiro, 2009, Stress-dependent anisotropy in transversely isotropic rocks: Comparison between theory and laboratory experiment on shale: Geophysics, **74**, 1, D7–D12, doi: 10.1190/1.3008546.

Doyen, P., 2007, Seismic reservoir characterization: An earth modeling perspective: EAGE.

Eberhart-Phillips, D., D.-H. Han, and M. D. Zoback, 1989, Empirical relationships among seismic velocity, effective pressure, porosity, and clay content in sandstone: Geophysics, **54**, 82–89, doi: 10.1190/1 .1442580.

Grechka, V. Y., P. A. Berge and J. G. Berryman, 1999, Analysis of Thomsen parameters for finely layered VT1 media: Geophysical Prospecting, **47**, 959–978.

Horne, S., Walsh, J., & Miller, D., 2012. Elastic anisotropy in the Haynesville Shale from dipole sonic data, First Break, **30**, 37–41.

Kaselow, A. and S. A. Shapiro, 2003, Application of the piezosensitivity approach: Changes of elastic moduli of isotropic and anisotropic porous rocks under isostatic loads: 73rd Annual International Meeting, SEG, Expanded Abstracts, 1624–1627.

Madadi, M., M. Pervukhina, and B. Gurevich, 2013, Modelling elastic anisotropy of dry rocks as a function of applied stress. Geophysical Prospecting. doi: 10.1111/1365-2478.12023.

Mavko, G., T. Mukerji, and J. Dvorkin, 2009, The rock physics handbook: Tools for seismic analysis of porous media, 2nd ed.: Cambridge University Press.

Ostadhassan, M., Z. Zeng, and H. Jabbari, 2012 Anisotropy Analysis in Shale Using Advanced Sonic Data - Bakken Case Study: Mehdi Search and Discovery Article #41049.

Pervukhina, M., B. Gurevich, P. Goloduniuc, and D. N. Dewhurst, 2011, Parameterization of elastic stress sensitivity in shales: Geophysics, 76, 3, WQ147–WA155, doi: 10.1190/1.3554401.

Prasad, M. and M. H. Manghnani, 1997, Effects of pore and differential pressure on compressional wave velocity and quality factor in Berea and Michigan sandstones: Geophysics, **62**, 1163–1176, doi: 10.1190/1.1444217.

Sava, 2004, Quantitative data integration for fracture characterization using statistical rock physics: PhD Thesis, Stanford University.

Sayers, C. M., 2012, The effect of anisotropy on the Young's moduli and Poisson's ratio of shales: Geophysical Prospecting, DOI: 10.1111/j.1365-2478.2012.01130.x

Sayers, C. M., 2005, Seismic anisotropy of shales: Geophysics, **64**, 93–98.

Sayers, C. M., 1994, The elastic anisotropy of shales: Journal of Geophysical Research-B, Solid Earth, **99**, 767–774.

Sayers, C. M. and M. Kachanov, 1995, Microcrack-induced elastic wave anisotropy of brittle rocks: Journal of Geophysical Research, **100**, 4149–4156.

Schoenberg, M., F. Muir, and C. M. Sayers, 1996, Introducing ANNIE: a simple three parameters anisotropic velocity model for shales, Journal of Seismic Exploration, **5**, 34–49.

Shapiro, S. A., 2003, Elastic piezosensitivity of porous and fractured rocks: Geophysics, **68**, 482–486, doi: 10.1190/1.1567215.

Siggins, A. F., and D. N. Dewhurst, 2003, Saturation, pore pressure and effective stress from sandstone acoustic properties: Geophysical Research Letters, **30**, 1089–1092.

Spikes, K. T., 2011, Modeling elastic properties and assessing uncertainty of fracture parameters in the Middle Bakken Siltstone: Geophysics, 76, 4, E117–E126, doi: 10.1190/1.3581129.

Stierman, D. J., J. H. Healy, and R. L. Kovach, 1979, Pressure-induced velocity gradient: An alternative to a Pg refractor in the Gabilan Range, central California: Bulletin of the Seismological Society of America, **69**, 397–415.

Thomsen, L., 1986, Weak elastic anisotropy: Geophysics, **51**, 1954–1966.

Tsvankin, I., 2001, Seismic signatures and analysis of reflection data in anisotropic media: New York: Pergamon.

Vernik, L., and X. Liu, 1997, Velocity anisotropy in shales - A petrophysical study: Geophysics, **62**, 521–532.

Wang, Z., 2002, Seismic anisotropy in sedimentary rocks, part 2: Laboratory data: Geophysics, **67**, 1423–1440.

Zimmerman, R. W., 1991, Compressibility of sandstones: Elsevier.